JM PAPERS

Reynolds number scaling and energy spectra in geostrophic convection

Matteo Madonia[1], **Andrés J. Aguirre Guzmán**[1], **Herman J.H. Clercx**[1] **and Rudie P.J. Kunnen**[1],†

[1]Fluids and Flows group, Department of Applied Physics and J. M. Burgers Centre for Fluid Dynamics, Eindhoven University of Technology, P.O. Box 513, 5600 MB Eindhoven, The Netherlands

We report flow measurements in rotating Rayleigh–Bénard convection in the rotationally constrained geostrophic regime. We apply stereoscopic particle image velocimetry to measure the three components of velocity in a horizontal cross-section of a water-filled cylindrical convection vessel. At a constant, small Ekman number $Ek = 5 \times 10^{-8}$, we vary the Rayleigh number Ra between 10^{11} and 4×10^{12} to cover various subregimes observed in geostrophic convection. We also include one non-rotating experiment. The scaling of the velocity fluctuations (expressed as the Reynolds number Re) is compared to theoretical relations expressing balances of viscous–Archimedean–Coriolis (VAC) and Coriolis–inertial–Archimedean (CIA) forces. Based on our results we cannot decide which balance is most applicable here; both scaling relations match equally well. A comparison of the current data with several other literature datasets indicates a convergence towards diffusion-free scaling of velocity as Ek decreases. However, at lower Ra, the use of confined domains leads to prominent convection in the wall mode near the sidewall. Kinetic energy spectra point at an overall flow organisation into a quadrupolar vortex filling the cross-section. This quadrupolar vortex is a quasi-two-dimensional feature; it manifests only in energy spectra based on the horizontal velocity components. At larger Ra, the spectra reveal the development of a scaling range with exponent close to $-5/3$, the classical exponent for inertial range scaling in three-dimensional turbulence. The steeper $Re(Ra)$ scaling at low Ek and development of a scaling range in the energy spectra are distinct indicators that a fully developed, diffusion-free turbulent bulk flow state is approached, sketching clear perspectives for further investigation.

Key words: turbulent convection, rotating turbulence

† Email address for correspondence: r.p.j.kunnen@tue.nl

1. Introduction

Buoyant convection and rotational influence through Coriolis acceleration are two principal features of fluid flows encountered in geophysics and astrophysics. A popular model system to study buoyant convective flows is Rayleigh–Bénard convection (RBC): a horizontal layer of fluid sandwiched between two parallel plates where the bottom plate is at a higher temperature than the top plate. With the inclusion of background rotation about a vertical axis, the problem of rotating Rayleigh–Bénard convection (RRBC) encompasses the principal actors, convection and rotation, in a simple, mathematically well-defined system amenable to experimental, numerical and analytical investigation. The interplay of convection and rotation is often studied in the RRBC context (Stevens, Clercx & Lohse 2013*a*; Kunnen 2021; Ecke & Shishkina 2023), which in itself has so far presented a wide variety of possible flow states without invoking additional complexities that may be encountered in geophysical and astrophysical flows such as magnetic fields, strong non-Oberbeck–Boussinesq effects, spherical geometries, and more (e.g. Jones 2011; Glatzmaier 2014; Aurnou *et al.* 2015; Schumacher & Sreenivasan 2020).

A property shared by the majority of geophysical and astrophysical flows is that they are characterised by large Reynolds numbers (ratio of inertial to viscous forces) and at the same time small Rossby numbers (ratio of inertial to Coriolis forces). We thus expect turbulent convective flow with a strong rotational constraint. In recent RRBC investigations, it was found that rotation-dominated convection – named the geostrophic regime after the dominant balance between Coriolis force and pressure gradient – displays an interesting subdivision into various realisable flow phenomenologies, each with specific scalings of descriptive statistical quantities like the efficiency of convective heat transfer (e.g. Sprague *et al.* 2006; Julien *et al.* 2012*b*; Ecke & Niemela 2014; Stellmach *et al.* 2014; Cheng *et al.* 2015, 2020; Lu *et al.* 2021; Madonia *et al.* 2021), which was reviewed recently in Kunnen (2021) and Ecke & Shishkina (2023). Starting from onset of convection, with increasing strength of buoyant forcing, one expects to encounter cellular convection, convective Taylor columns (CTCs), plumes and geostrophic turbulence (GT), showing step by step a decreasing rotational constraint (Sprague *et al.* 2006; Julien *et al.* 2012*b*; Kunnen 2021; Aguirre Guzmán *et al.* 2022). From our prior heat transfer and temperature measurements (Cheng *et al.* 2020), we could identify an additional transitional state, rotation-influenced turbulence (RIT), that requires further description.

Getting to the geostrophic regime requires dedicated tools: large-scale experimental set-ups (e.g. Ecke & Niemela 2014; Cheng *et al.* 2015, 2018, 2020; Hawkins 2020; Lu *et al.* 2021; Hawkins *et al.* 2023), direct numerical simulations (DNS) on fine meshes (e.g. Stellmach *et al.* 2014; Aguirre Guzmán *et al.* 2020) or asymptotically reduced modelling (e.g. Sprague *et al.* 2006; Julien *et al.* 2012*b*; Maffei *et al.* 2021). A complicating factor for experiments in particular is that at the confining sidewall, a prominent mode of convection is formed, named the wall mode, boundary zonal flow or sidewall circulation (Favier & Knobloch 2020; de Wit *et al.* 2020; Zhang *et al.* 2020; Lu *et al.* 2021; Zhang, Ecke & Shishkina 2021; Ecke, Zhang & Shishkina 2022; Wedi *et al.* 2022). This convection mode is the first to become unstable to buoyant forcing, before bulk convection (e.g. Zhang & Liao 2009), and was found unexpectedly to persist deep into the turbulent regimes (Madonia *et al.* 2021). This complicates the interpretation of results on global flow properties (like the efficiency of convective heat transfer) and their comparison to studies without lateral confinement (i.e. simulations on domains with periodic boundary conditions).

The difficulty of entering the geostrophic regime, particularly for experiments and DNS, leaves it scarcely studied with many open questions remaining, particularly considering

the statistical description of this turbulent flow from velocity measurements. Here, we contribute flow measurements from our dedicated experimental setup TROCONVEX (Cheng *et al.* 2018, 2020; Madonia *et al.* 2021). At a constant rotation rate, we choose different strengths of buoyant forcing to scan the subranges of the geostrophic regime. We quantify the strength of turbulence in terms of the Reynolds number, and compute kinetic energy spectra to identify the distribution of energy over the spatial scales.

The remainder of this paper is organised as follows. In §2, we introduce the dimensionless input and output parameters of RRBC, and list proposed scaling arguments for the Reynolds number. Then the experimental methods are explained in §3. Results on the measured Reynolds numbers are given in §4, along with a test of the scaling arguments and a comparison to literature data. In §5, we plot and discuss the computed kinetic energy spectra. We present our conclusions in §6.

2. Theoretical background

We will first define the dimensionless input and output parameters of RRBC in §2.1. Then the effects of rotation on the stability of convective flow are treated in §2.2. In §2.3, we discuss scaling arguments for the Reynolds number proposed in the literature.

2.1. *Input and output parameters*

Three dimensionless input parameters are required to describe the flow state. The Rayleigh number *Ra* expresses the ratio of thermal forcing to dissipation, the Ekman number *Ek* is the ratio of viscous to Coriolis forces, and the Prandtl number *Pr* describes the diffusive properties of the fluid. These quantities are defined as

$$Ra = \frac{g\alpha\,\Delta T\,H^3}{\nu\kappa}, \quad Ek = \frac{\nu}{2\Omega H^2} \quad Pr = \frac{\nu}{\kappa}, \tag{2.1a–c}$$

where g is gravitational acceleration, ΔT the applied temperature difference between the plates and H is their vertical separation, Ω is the rotation rate, and α, ν and κ are the thermal expansion coefficient, kinematic viscosity and thermal diffusivity of the fluid, respectively. A related parameter that has been used frequently to give an *a priori* indication of the relative importance of buoyant forcing to Coriolis forces (see e.g. Stevens *et al.* 2013*a*; Aurnou, Horn & Julien 2020; Kunnen 2021; Ecke & Shishkina 2023) is the so-called convective Rossby number

$$Ro_c = \frac{U_{ff}}{2\Omega H} = Ek\sqrt{\frac{Ra}{Pr}}, \tag{2.2}$$

where the free-fall velocity $U_{ff} = \sqrt{g\alpha\,\Delta T\,H}$ indicates the maximum flow speed that could develop in this convection system.

Two prominent output parameters are the Nusselt number *Nu* and the Reynolds number *Re*, which indicate the efficiency of convective heat transfer and momentum transfer, respectively. The Nusselt number is defined as

$$Nu = \frac{q}{q_{cond}} = \frac{qH}{\lambda\,\Delta T}. \tag{2.3}$$

The total heat flux q (convection and conduction) is normalized by the conductive flux $q_{cond} = \lambda\,\Delta T/H$, with λ the thermal conductivity of the fluid. In the absence of convection (a quiescent fluid), $q = q_{cond}$ and $Nu = 1$; when convection sets in, $q > q_{cond}$ and $Nu > 1$.

In our current configuration, with gravity pointing downwards, the total heat flux can be expressed as

$$q = \frac{\lambda}{\kappa} \langle wT \rangle - \lambda \left\langle \frac{\partial T}{\partial z} \right\rangle, \tag{2.4}$$

where z is the vertical coordinate pointing upwards, counter to gravity, and w is the vertical component of velocity. Angular brackets $\langle \cdot \rangle$ denote a suitable average, either a cross-sectional plane average at a certain height z, or a volume average over the flow domain. The Reynolds number

$$Re = \frac{UH}{\nu} \tag{2.5}$$

introduces a characteristic velocity scale U, usually taken to be the root-mean-square (r.m.s.) velocity. The ultimate goal is to understand how Nu and Re depend on the input parameters Ra, Pr and Ek. Power-law scaling relations are expected (e.g. Julien *et al.* 2012*a*; King, Stellmach & Buffett 2013; Maffei *et al.* 2021). For non-rotating convection, the phenomenological theory developed by Grossmann & Lohse (2000, 2001, 2002, 2004) (see also Ahlers, Grossmann & Lohse 2009; Stevens *et al.* 2013*b*) has been very successful in explaining the $Nu(Ra, Pr)$ and $Re(Ra, Pr)$ relations.

2.2. *Stabilisation of convection by rotation*

Rotation tends to stabilise convection. For $Pr > 0.68$ and at asymptotically small $Ek \to 0$, linear stability theory (Chandrasekhar 1961; Niiler & Bisshopp 1965) predicts the critical Rayleigh number Ra_C for onset of convection, and the characteristic horizontal size ℓ_C of convection near onset (half the most unstable wavelength), as

$$Ra_C = 8.70 \, Ek^{-4/3}, \quad \ell_C/H = 2.41 \, Ek^{1/3}. \tag{2.6a,b}$$

(The onset of convection for $Pr < 0.68$ behaves differently (Chandrasekhar 1961; Aurnou *et al.* 2018); it is out of scope for the current investigation.) Due to this stabilising effect, it is insightful to also consider the degree of supercriticality Ra/Ra_C to get a first impression of the intensity of convection. These asymptotic formulations are accurate for this work given the small applied Ek.

2.3. *Reynolds number scaling in rotating convection*

Several scaling relations for the Reynolds number have been proposed for RRBC flow. They are based on balancing terms in the governing Navier–Stokes equation for an incompressible Oberbeck–Boussinesq fluid, which is (e.g. Chandrasekhar 1961)

$$\frac{\partial \boldsymbol{u}}{\partial t} + (\boldsymbol{u} \cdot \nabla)\boldsymbol{u} = -\nabla p - 2\Omega \hat{\boldsymbol{z}} \times \boldsymbol{u} + \nu \nabla^2 \boldsymbol{u} + g\alpha T \hat{\boldsymbol{z}}, \quad \nabla \cdot \boldsymbol{u} = 0. \tag{2.7}$$

This equation describes the evolution of velocity $\boldsymbol{u}$ as a function of time t, where p is the reduced pressure (e.g. Greenspan 1968; Kundu & Cohen 2002) and T is temperature; $\hat{\boldsymbol{z}}$ is the vertical unit vector pointing upwards, counter to gravity. Centrifugal buoyancy is excluded here (Horn & Aurnou 2018, 2019). The equation for vorticity $\boldsymbol{\omega} = \nabla \times \boldsymbol{u}$ is also

962 A36-4

invoked in these scaling arguments:

$$\frac{\partial \boldsymbol{\omega}}{\partial t} + (\boldsymbol{u} \cdot \boldsymbol{\nabla})\boldsymbol{\omega} = (\boldsymbol{\omega} \cdot \boldsymbol{\nabla})\boldsymbol{u} + 2\Omega \frac{\partial \boldsymbol{u}}{\partial z} + \nu \nabla^2 \boldsymbol{\omega} - g\alpha \hat{\boldsymbol{z}} \times \boldsymbol{\nabla} T. \tag{2.8}$$

One proposed scaling relation balances the viscous, buoyancy and Coriolis terms into the so-called viscous–Archimedean–Coriolis (VAC) balance (Aubert *et al.* 2001; Gillet & Jones 2006; King *et al.* 2013). First, we recall the exact global balance of energy (viscous dissipation equals buoyant production) that can be found by averaging the energy equation $\boldsymbol{u}\cdot$ (2.7) over the flow domain (Shraiman & Siggia 1990; Grossmann & Lohse 2000; Ahlers *et al.* 2009):

$$\nu \langle (\boldsymbol{\nabla} \boldsymbol{u})^2 \rangle_V = g\alpha \langle wT \rangle_V = \frac{\nu^3}{H^4} \frac{Ra\,(Nu - 1)}{Pr^2}, \tag{2.9}$$

where $\langle \cdot \rangle_V$ denotes a volume average. For modest convection, geostrophy and the Taylor–Proudman theorem are considered to be broken by viscosity acting on small horizontal scales. The balance of viscous and Coriolis terms in the vorticity equation is scaled by recognising that vertical derivatives $\partial/\partial z$ scale as $1/H$, and horizontal derivatives $\partial/\partial x$ and $\partial/\partial y$ scale as $1/\ell$, where $\ell \ll H$ is the horizontal scale of convection:

$$2\Omega \frac{\partial \boldsymbol{u}}{\partial z} \sim \nu \nabla^2 \boldsymbol{\omega} \rightarrow 2\Omega \frac{U}{H} \sim \nu \frac{U}{\ell^3} \rightarrow \frac{\ell}{H} \sim \left(\frac{\nu}{2\Omega H^2} \right)^{1/3} = Ek^{1/3}. \tag{2.10}$$

We recover the scaling of the onset length scale ℓ_C of (2.6*a,b*), which is a consequence of this VAC force balance. Using $\boldsymbol{\nabla} \sim 1/\ell$ (i.e. dominated by the horizontal derivatives), we can scale the first term in (2.9) as $\nu U^2/\ell^2$, then, using (2.10), rewrite it in terms of the Reynolds number as

$$\nu \frac{U^2}{\ell^2} \sim \frac{\nu^3}{H^4} \frac{Ra\,(Nu - 1)}{Pr^2} \rightarrow Re_{VAC} \sim \frac{Ra^{1/2}\,Ek^{1/3}\,(Nu - 1)^{1/2}}{Pr}. \tag{2.11}$$

A second proposed scaling is built on a balance of Coriolis–inertial–Archimedean (CIA) forces (Ingersoll & Pollard 1982; Aubert *et al.* 2001; Jones 2011; Guervilly, Cardin & Schaeffer 2019; Aurnou *et al.* 2020). For a fully turbulent flow, effects of viscosity are negligible at larger length scales, and Coriolis and inertial forces are balanced in the vorticity equation

$$2\Omega \frac{\partial \boldsymbol{u}}{\partial z} \sim (\boldsymbol{u} \cdot \boldsymbol{\nabla})\boldsymbol{\omega} \rightarrow 2\Omega \frac{U}{H} \sim \frac{U^2}{\ell^2} \rightarrow \frac{\ell}{H} \sim \left(\frac{U}{2\Omega H} \right)^{1/2} = Ro^{1/2}, \tag{2.12}$$

where the horizontal length scale ℓ now scales as the square root of the Rossby number $Ro = U/(2\Omega H)$ based on the velocity scale U (Guervilly *et al.* 2019). Then inertia and buoyancy are balanced in the energy equation

$$\boldsymbol{u} \cdot ((\boldsymbol{u} \cdot \boldsymbol{\nabla})\boldsymbol{u}) \sim g\alpha \boldsymbol{u} \cdot (T\hat{\boldsymbol{z}}) \rightarrow \frac{U^3}{\ell} \sim \frac{\nu^3}{H^4} \frac{Ra\,(Nu - 1)}{Pr^2}, \tag{2.13}$$

where (2.9) has been used, invoking a volume average. The final scaling relation, combining (2.12) and (2.13), can be rewritten in terms of *Re* as

$$Re_{CIA} \sim \frac{Ra^{2/5}\,Ek^{1/5}\,(Nu - 1)^{2/5}}{Pr^{4/5}}. \tag{2.14}$$

What remains to be determined is the dependence of the Nusselt number *Nu* on the input parameters. For rotating convection, this relation is far from complete, with a variety

of subregimes opening up in the geostrophic regime based on recent numerical and experimental evidence (Sprague *et al.* 2006; Julien *et al.* 2012*b*; Ecke & Niemela 2014; Cheng *et al.* 2015, 2018, 2020; Kunnen 2021; Lu *et al.* 2021). Two theoretical scalings have been proposed.

The first scaling (Boubnov & Golitsyn 1990; King *et al.* 2009; King, Stellmach & Aurnou 2012) is a rotating equivalent of Malkus's marginal stability argument for the thermal boundary layer (Malkus 1954): the Rayleigh number Ra_δ based on the thickness δ of the thermal boundary layer exceeds its critical value $Ra_{\delta,C} \sim Ek_\delta^{-4/3}$ with an Ekman number also based on δ. With the assumption of a temperature drop $\Delta T_\delta \sim \Delta T$ over a thermal boundary layer that is purely conductive ($q \sim \lambda \Delta T/\delta$), King *et al.* (2009, 2012) find

$$Nu \sim \left(\frac{Ra}{Ra_C} \right)^3 \sim Ra^3 \, Ek^4. \tag{2.15}$$

This scaling relation was also derived by Boubnov & Golitsyn (1990) based on measurements of the vertical mean temperature profile.

The second scaling relation is a rotating equivalent of Spiegel's argument that under vigorously turbulent conditions, the heat flux q should become independent of the diffusive fluid properties ν and κ (Spiegel 1971). Stevenson (1979) and Julien *et al.* (2012*a*) show that if rotation is included, the only combination of parameters leading to diffusion-free total heat flux q is

$$Nu - 1 \sim \frac{Ra^{3/2} \, Ek^2}{Pr^{1/2}}. \tag{2.16}$$

Numerical and experimental evidence points towards the asymptotic validity of the latter scaling (2.16) (Julien *et al.* 2012*a*; Stellmach *et al.* 2014; Bouillaut *et al.* 2021), although the presence of no-slip walls (Stellmach *et al.* 2014; Kunnen *et al.* 2016; Plumley *et al.* 2017; Aguirre Guzmán *et al.* 2021) and the significant heat flux contribution of the wall mode near sidewalls in confined convection (Favier & Knobloch 2020; de Wit *et al.* 2020; Zhang *et al.* 2020, 2021; Lu *et al.* 2021; Ecke *et al.* 2022) preclude observation of the pure scaling law.

Upon insertion of (2.16) into (2.14), we obtain in dimensionless and dimensional form that

$$Re \sim \frac{Ra \, Ek}{Pr} \rightarrow U \sim \frac{g\alpha \, \Delta T}{2\Omega}, \tag{2.17}$$

i.e. the velocity scale U is now also diffusion-free (Aurnou *et al.* 2020).

3. Experimental methods

The experimental set-up used for this study is TROCONVEX, a large-scale rotating convection apparatus designed for the study of the geostrophic regime of convection. The design considerations with regard to the accessible parameter range for a given set-up have been discussed in detail in Cheng *et al.* (2018). Details on the set-up for heat transfer measurements are given in Cheng *et al.* (2020). Here, we perform optical flow measurements using stereoscopic particle image velocimetry (stereo-PIV; Prasad 2000; Raffel *et al.* 2007). The arrangement has been explained in Madonia *et al.* (2021); here, we repeat the most important parts.

The convection cell is an upright cylinder of height $H = 2$ m and radius $R = 0.195$ m filled with water. Its diameter-to-height aspect ratio is $\Gamma = 2R/H = 0.195$. The bottom plate is made of copper and is heated electrically to be at a controlled temperature T_b.

ΔT (°C)	$Ra/10^{12}$	$Ek \times 10^8$	Ra/Ra_C	$Re_u/10^3$	$Re_w/10^3$
0.50	0.108	5.00	2.29	3.10 ± 0.21	2.31 ± 0.27
1.00	0.216	5.00	4.57	3.09 ± 0.25	2.18 ± 0.20
2.00	0.432	5.00	9.14	3.88 ± 0.20	2.63 ± 0.31
3.00	0.648	5.00	13.7	5.80 ± 0.80	3.43 ± 0.31
5.00	1.08	5.00	22.9	7.93 ± 0.95	5.60 ± 0.48
10.0	2.16	5.00	45.7	12.88 ± 0.88	8.66 ± 0.46
20.0	4.32	5.00	91.4	17.67 ± 0.92	12.90 ± 1.16
3.00	0.648	∞	$O(10^8)$	10.34 ± 1.61	13.66 ± 2.59

Table 1. Parameter values for the experiments. In all cases, $\Gamma = 0.195$ and $Pr = 5.2$. Output parameters are the Reynolds numbers Re_u and Re_w based on horizontal and vertical r.m.s. velocities, respectively. For the non-rotating experiment (bottom row), the parameter Ra/Ra_C is not stated explicitly. It is large given that without rotation Ra_C is only $O(10^3)$; quantitative comparison to the rotating cases is not meaningful.

Likewise, the temperature of the copper top plate, equipped with a double-spiral groove for cooling liquid circulation, is controlled to a temperature T_t by a combination of a chiller and a thermostated bath. The mean temperature $T_m = (T_b + T_t)/2$ is kept at a constant 31 °C, so that $Pr = 5.2$. The convection cell is placed on a rotating table. We apply constant rotation $\Omega = 1.93$ rad s^{-1}, corresponding to $Ek = 5.00 \times 10^{-8}$. At this Ekman number, $2R/\ell_C \approx 22$, i.e. the cylinder diameter fits 22 times the characteristic onset length ℓ_C. The temperature difference $\Delta T = T_b - T_t$ is changed between experiments to vary Ra. Additionally, one non-rotating experiment is included for reference. The operating conditions for the various experiments are summarised in table 1. These conditions are the same as in Madonia *et al.* (2021); they also overlap with the heat transfer data from the same set-up reported in Cheng *et al.* (2020), at the intermediate Ek value considered in that paper.

Optical access is facilitated by a custom-made water-filled prism mounted around the cylinder, significantly reducing refraction on the cylinder wall. It allows for horizontal crossing of a laser light sheet with thickness approximately 3.5 mm at mid-height $z/H = 0.5$. The laser pulses at frequencies 7.5 or 15 Hz, depending on the typical flow speeds. The water is seeded with polyamid particles with nominal diameter 5 μm. Two 5 Mpixel cameras (Jai SP-500M-CXP2) equipped with Scheimpflug adapters are each placed at a stereoscopic angle of approximately 45° with the vertical, so that stereo-PIV can be applied (Prasad 2000; Raffel *et al.* 2007). We can measure the full velocity vectors $\boldsymbol{u} = (u, v, w)$ in the laser light sheet plane, resulting in a grid of vectors with separation 3.2 mm in both horizontal directions that fits 122 vectors in the cylinder diameter. Between 3000 and 9000 vector fields are evaluated per experiment, for a measurement duration ranging from 200 to 600 s.

Results are presented in terms of Reynolds numbers. Horizontal and vertical velocities are treated separately. The Reynolds number Re_u is based on the characteristic horizontal velocity $U_h = \sqrt{\langle u^2 \rangle + \langle v^2 \rangle}$. Here, $\langle \cdot \rangle$ denotes either averaging over time and over circular shells to obtain radial profiles, or averaging over time and over the full cross-sectional area excluding the wall mode near the sidewall (to be defined more precisely later on) to get to a single representative value per experiment. In this azimuthal averaging, we divide the section into 65 concentric circular shells. Each shell represents a ring of thickness 3 mm, comparable to the resolution of our PIV vector field spacing (3.2 mm). Similarly, Re_w is based on the characteristic velocity scale $W = \sqrt{\langle w^2 \rangle}$. In all
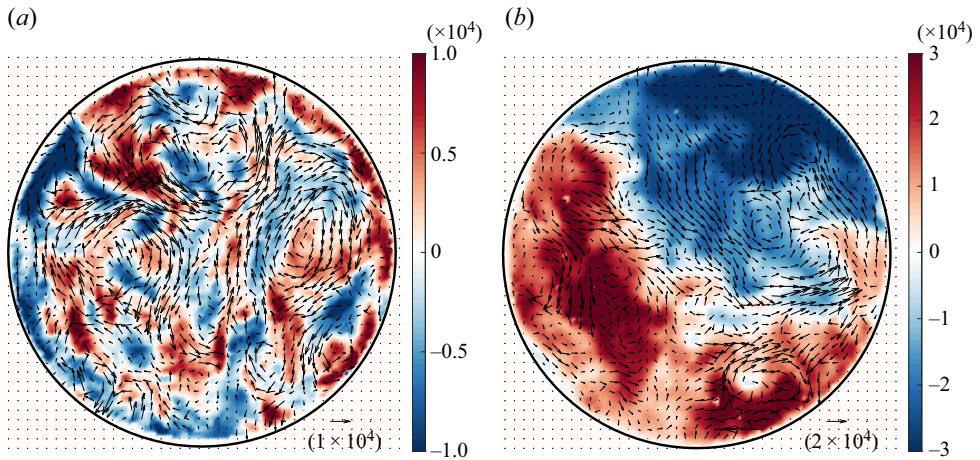
Figure 1. Instantaneous velocity snapshots at $Ra = 6.48 \times 10^{11}$: (*a*) with rotation, $Ek = 5.00 \times 10^{-8}$; (*b*) no rotation, $Ek = \infty$. The arrows display the horizontal velocity components; for clarity, only one-ninth of the total number of vectors is displayed. The background colour indicates the vertical velocity component. Velocities are normalised with the viscous velocity $\nu/H = 3.87 \times 10^{-7}$ m s^{-1}.

cases, $\langle u \rangle \approx \langle v \rangle \approx \langle w \rangle \approx 0$. These Reynolds numbers can also be interpreted as the r.m.s. velocities normalised with the viscous velocity scale $U_\nu = \nu/H$. Likewise, we consider the r.m.s. value of the vertical component of vorticity, ω_z^{rms}.

An important consideration that is encountered in rotating convection experiments is the effect of centrifugal buoyancy (Horn & Aurnou 2018, 2019). We use the Froude number $Fr = \Omega^2 R/g$ to quantify the ratio of maximal centrifugal to gravitational acceleration. Since centrifugal acceleration is negligibly small in most geophysical and astrophysical applications, its effects (as studied in detail by Horn & Aurnou 2018, 2019) should preferably be kept to a minimum in experiments, i.e. $Fr \ll 1$. Here, $Fr = 0.074$ for all rotating experiments. Such a *Fr* value did not lead to significant up/down asymmetry in our sidewall temperature measurements (Cheng *et al.* 2020); we expect that centrifugal buoyancy is negligibly small in these experiments, too.

To give a first impression of the measurement results, we plot two instantaneous velocity field snapshots at $Ra = 6.48 \times 10^{11}$, with and without rotation, in figure 1. Velocities are normalised with the viscous velocity scale ν/H, which is 3.87×10^{-7} m s^{-1} at this mean temperature. As such, the magnitude of the normalised velocity components in these plots can be interpreted as displaying the local instantaneous Reynolds number. It is clear that rotation, present in figure 1(*a*) but absent in figure 1(*b*), has a large effect on the overall flow structuring. Under rotation, the flow tends to organise into structures that are considerably smaller than the diameter of the cylinder, while without rotation, the global organisation is as large as the cross-section. We have considered the characteristic size of the flow features before in Madonia *et al.* (2021), where we could see that the correlation length for vertical velocity increases as *Ra* grows. In the rotating experiments, we can also observe intense vertical motion near the sidewall due to the convective wall mode (Favier & Knobloch 2020; de Wit *et al.* 2020; Zhang *et al.* 2020, 2021; Lu *et al.* 2021; Ecke *et al.* 2022). For roughly half of the circumference, we find upward flow close to the sidewall; the other half is downward. In the non-rotating experiment (figure 1*b*), the large-scale circulation is observed (e.g. Ahlers *et al.* 2009): a vertical convection roll filling the domain with one half upward flow and one half downward flow.
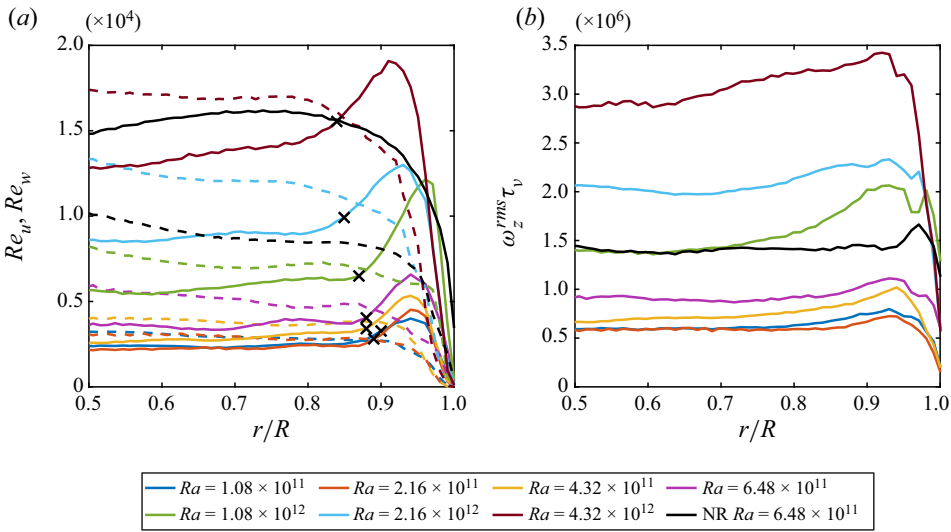
962 A36-8

Figure 2. (*a*) Radial dependence of Re_u (dashed lines) and Re_w (solid lines) for different Ra. Black crosses indicate the beginning of the sidewall boundary layer, following 4.1. (*b*) Radial dependence of ω_z^{rms} for different Ra, normalised using the viscous time scale $\tau_\nu = H^2/\nu$. The legend entry 'NR' refers to the non-rotating experiment. All the quantities displayed in this figure are shown from only half the cylinder radius onwards for clarity.

4. Reynolds number results

4.1. *Radial profiles*

We first consider radial profiles of the Reynolds numbers Re_u and Re_w, plotted in figure 2(*a*). Both quantities show an overall trend of larger values for larger Ra, as expected, with the exception of the two lowest Ra cases, which are almost identical. The distinction between an inner and a near-wall outer portion of the domain is clear from both quantities: both profiles suggest a generally constant value that is largely independent of the radial position for the bulk part, away from the lateral sidewall, and a change of behaviour close to this sidewall. There, we see an increase in Re_w, a clear indication of the presence of vigorous convection near the sidewall in the wall mode. The black crosses in figure 2(*a*) indicate the approximate thickness of the sidewall boundary layer following the empirical relation

$$\delta_{w_{rms}}/R = a\,Ra^{0.15\pm0.02}, \tag{4.1}$$

based on capturing the radial extent of the near-wall w_{rms} peak; $a = (3 \pm 1) \times 10^{-3}$ is reported by de Wit *et al.* (2020). Here we use $a = 2 \times 10^{-3}$ as the prefactor and 0.15 as the exponent for Ra. This definition agrees well with our data as it indicates the extent of the sidewall layer, in both Re_w and Re_u. For the former, it is at the base of the near-wall peak; for the latter, we see the beginning of the decay to zero.

The non-rotating case (black curves in figure 2*a*) shows three main points of interest. First, Re_w displays an immediate decay to zero close to the sidewall without any previous increase, contrary to the rotating cases. Second, without rotation, we measure significantly higher values of both Re_u and Re_w relative to the rotating case at the same Ra (compare black and purple curves in figure 2*a*), a clear indication that the strong influence of rotation makes the flow less turbulent, suppressing both vertical and horizontal r.m.s. velocities.
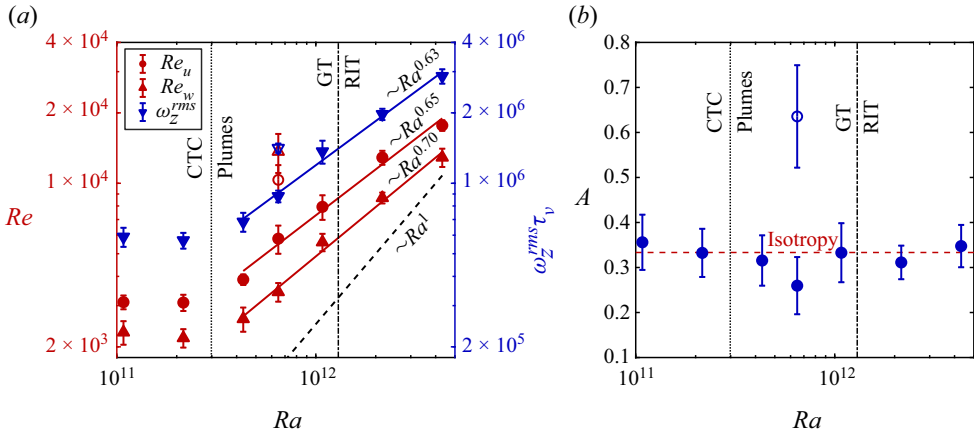
Figure 3. (*a*) Dependence on *Ra* of Reynolds numbers based on horizontal (Re_u) and vertical (Re_w) velocity components (red, left ordinate) and vertical vorticities ω_z^{rms} (blue, right ordinate). Vorticity is normalised with the viscous timescale $\tau_\nu = H^2/\nu$. The solid lines represent power-law fits $Re_u \sim Ra^{0.65\pm0.07}$, $Re_w \sim Ra^{0.70\pm0.06}$ and $\omega_z^{rms} \sim Ra^{0.63\pm0.05}$. The dashed black diagonal line indicates the scaling $Re \sim Ra$ for reference. (*b*) Kinetic energy anisotropy $A = W^2/(U_h^2 + W^2)$ versus *Ra*. For isotropy, $A = \frac{1}{3}$ (red dashed line). In both panels, the dotted and dash-dotted lines represent the transitional *Ra* between CTCs and plumes, and between GT and RIT, respectively, while open symbols represent the values for the non-rotating case.

Third, the r.m.s. vertical velocity is now considerably more pronounced than the horizontal component, unlike the rotating cases. We will discuss flow anisotropy later in this paper.

In figure 2(*b*), we plot ω_z^{rms} normalised using the viscous time scale $\tau_\nu = H^2/\nu$. The same trends as for Re_w are reflected here, with the two cases with lowest *Ra* being almost identical, and profiles that increase for higher *Ra*. Also here, we see higher values for the non-rotating case compared to its corresponding rotating counterpart, even though the difference is less than we see for vertical velocities. The non-rotating case also shows a localised peak close to the sidewall, while the rotating cases have a wider radial region where the vorticity increases before dropping down at the wall.

All the quantities displayed in figure 2 are shown from half the cylinder radius onwards, for clarity. The inner part keeps showing a constant behaviour down to approximately $\frac{1}{10}R$, a circle of approximately 20 mm around the axis of the cylinder, where the scarcity of velocity vectors prevents meaningful radial binning and azimuthal averaging.

The quantities Re_u, Re_w and ω_z^{rms} are approximately constant in the inner part of the cylinder. From the profiles in figure 2, we can extract for every *Ra* a mean value of that quantity in the bulk. This bulk average is obtained by excluding the wall zone as defined by (4.1) as well as excluding a circle of radius 20 mm from the cylinder axis, an area where the azimuthal averaging does not give trustworthy data, as argued above. In figure 3(*a*), we plot these averaged data as a function of *Ra*, with error bars that represent the standard deviations of these means. We also give the corresponding flow states as inferred from our earlier heat transfer measurements (Cheng *et al.* 2020).

As mentioned before, the two lower *Ra* cases, both in the CTC regime, show very similar values. From the plumes regime onwards, all the quantities display a steeper trend that is reasonably constant between the plumes/GT and RIT states: $Re_u \sim Ra^{0.65\pm0.07}$, $Re_w \sim Ra^{0.70\pm0.06}$ and $\omega_z^{rms} \sim Ra^{0.63\pm0.05}$. These exponents are notably smaller than the diffusion-free velocity scaling $Re \sim Ra$ of (2.17) included in figure 3 with a dashed black line. At the same time, these exponents are notably larger than the non-rotating

trend $Re \sim Ra^{0.44}$ that has been measured in various experiments and employing different methods, as summarised by Ahlers *et al.* (2009). They are even larger than the 'ultimate' diffusion-free scaling $Re \sim Ra^{1/2}$ for non-rotating convection (Kraichnan 1962; Spiegel 1971; Grossmann & Lohse 2002). Another clear difference between the current non-rotating and rotating experiments is that without rotation, the values are higher than with rotation at the same *Ra*.

The vorticity scaling $\omega_z^{rms} \sim Ra^{0.63}$ follows nicely that of horizontal velocity. From this information, we can infer that the characteristic horizontal length scale ℓ does not change much with *Ra*, employing the estimate $\omega_z \sim U_h/\ell$. This *Ra*-independent characteristic scale for rapidly rotating convection is one of the starting points of the asymptotically reduced equations (e.g. Sprague *et al.* 2006; Julien *et al.* 2012*b*) that describe the flow in the limit $Ek \rightarrow 0$ and that have provided a lot of insights into geostrophic convection. We have measured correlation length scales before, in Madonia *et al.* (2021). While velocity-based correlation lengths grew with increasing *Ra*, the correlation lengths based on vertical vorticity (which can be interpreted as the Taylor microscale) were found to be largely independent of *Ra*. Taylor length scales independent of *Ra* have also been observed in asymptotic plane layer dynamo simulations by Yan & Calkins (2022).

To study the degree of anisotropy in the bulk flow, we plot in figure 3(*b*) the kinetic energy anisotropy for each case, defined as

$$A = \frac{W^2}{U_h^2 + W^2}. \tag{4.2}$$

It describes the fraction of total kinetic energy found in vertical motions. In the isotropic case, where the energy is distributed equally among the three components, this value would be $\frac{1}{3}$. As we see from figure 3(*b*), the non-rotating case is far away from that value, while the rotating cases display values very close to the isotropic one, with the possible exception of the case with $Ra = 6.48 \times 10^{11}$, possibly a point of transition between the plumes and GT states of the geostrophic regime, for which no transition relation is currently available. Here, rotation thus suppresses the large anisotropy of non-rotating convection, ending up in near-isotropy.

4.2. *Test of force balance scaling relations*

We can use the measured characteristic velocities to test compliance (in terms of *Ra* scaling) with the scaling relations (2.11) and (2.14), respectively based on the VAC and CIA force balances. We graphically test the compliance in figure 4 by plotting Re/Re_{VAC} and Re/Re_{CIA}. Input on the *Nu*(*Ra*) scaling is required. Here, we use our prior heat transfer results obtained in the same experimental set-up by Cheng *et al.* (2020), namely, $Nu \sim Ra^{0.64}$ for the plumes/GT range, and $Nu \sim Ra^{0.52}$ for the RIT range. It must be emphasised that these measured relations may be affected by the heat transfer contribution of the sidewall circulation (de Wit *et al.* 2020; Zhang *et al.* 2020; Lu *et al.* 2021). We also include the ultimate scaling $Nu \sim Ra^{3/2}$ as per (2.16). The VAC scaling test is included for this diffusion-free relation, too, despite the incompatibility of combining a diffusion-free *Nu* scaling with a force balance that includes the viscous force explicitly. The *Re* scaling relations (2.11) and (2.14) do not have numerical prefactors. To make these plots, we have chosen the prefactors such that the points are at the same level on average for ease of comparison.

For both Re_u and Re_w, it is observed that either VAC or CIA scaling does a good job of describing the results, provided that our earlier experimental *Nu*(*Ra*) relations
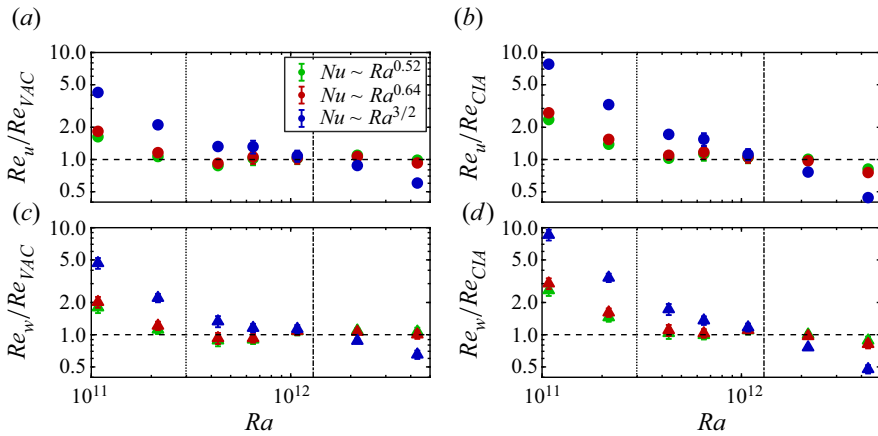
Figure 4. Test of $Re(Ra)$ scaling with VAC (see (2.11)) and CIA (see (2.14)) force balance arguments, for (a,b) Re_u, and (c,d) Re_w. Three different $Nu(Ra)$ relations are invoked: $Nu \sim Ra^{0.52}$ (green, for RIT) and $Nu \sim Ra^{0.64}$ (red, for plumes/GT) based on our heat transfer measurements in the same set-up (Cheng *et al.* 2020), and $Nu \sim Ra^{3/2}$ (blue) following (2.16).

are employed. We see that both relations $Nu \sim Ra^{0.52}$ and $Nu \sim Ra^{0.64}$ lead to comparable results and are equally valid in the plumes/GT and RIT ranges. Based on these plots and on the current data, we cannot decide which scaling (VAC or CIA) is most appropriate. This is in line with the analysis of Hawkins *et al.* (2023) (also covered in Hawkins 2020), who similarly reported co-scaling of VAC and CIA relations based on measurements using laser Doppler velocimetry. We can insert these numbers into the scaling relations (2.11) and (2.14) for a quantitative comparison. Using $Nu \sim Ra^{0.64}$ for the plumes/GT range, we arrive at the prediction $Re \sim Ra^{0.82}$ from VAC scaling, and $Re \sim Ra^{0.66}$ from the CIA balance. When we use $Nu \sim Ra^{0.52}$ as obtained for the RIT range, we find $Re \sim Ra^{0.76}$ for VAC, and $Re \sim Ra^{0.61}$ for CIA. Our exponents for the velocity scalings from figure 3 are in this range – perhaps a bit closer to the CIA trend than to the VAC scaling, but certainly not giving a conclusive answer either. We are probably in a state where both inertial and viscous forces play a role. The flow is turbulent enough that inertial forces are relevant, but not yet turbulent enough to reach the diffusion-free scaling $Re \sim Ra$ of (2.17). Hawkins *et al.* (2023) conclude that pure CIA scaling is not observed given that the $Nu(Ra)$ is still affected by boundary-layer dynamics and thus not diffusion-free yet – a result that we share (Cheng *et al.* 2020).

To interpret our data further and compare to previously published results, we collect several reported datasets for Re_w in figure 5. We plot $\widetilde{Re}_w = Re_w\,Ek^{1/3}$ as a function of $(\widetilde{Ra} - \widetilde{Ra}_C)/Pr = (Ra - Ra_C)\,Ek^{4/3}/Pr$, both inspired and necessitated by the results of Maffei *et al.* (2021) from asymptotic model simulations. In their asymptotic equation, $Ek \to 0$ so Ek itself remains undefined. Furthermore, using this plot convention, they obtained a good collapse of their data spanning a range of Pr and $\widetilde{Ra}$; see the plus symbols in the plot. Their simulation domain is a Cartesian box with periodic boundary conditions in the horizontal directions and stress-free walls on bottom and top. The other datasets are from DNS and experiments, where the corresponding Ekman number is colour-coded. The current results are included with diamonds. The experimental results by Hawkins *et al.* (2023) cover a significant range $Ra \approx 10^8$–2×10^{11} and $Ek \approx 10^{-7}$–3×10^{-5}; they are the reported RRBC Reynolds number data closest to the current study in terms of Ra and Ek,
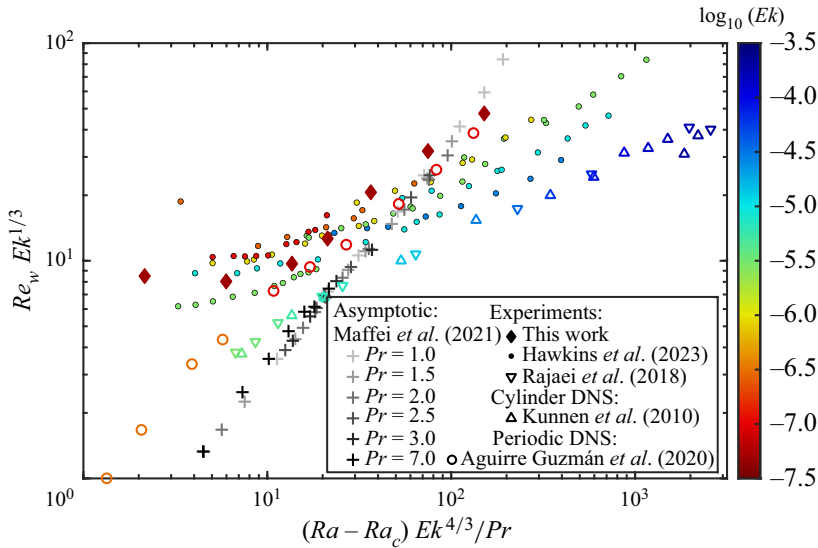
962 A36-12

Figure 5. Comparison of current results for Re_w with published results. Plus signs: data from Maffei *et al.* (2021), colour coded by Pr, results from asymptotically reduced model simulations on a horizontally periodic domain. Other symbols colour-coded by Ek (see colour bar). Diamonds: current results. Small filled circles: experiments of Hawkins *et al.* (2023). Up triangles: DNS in a cylinder (Kunnen *et al.* 2010). Down triangles: experiments of Rajaei *et al.* (2018). Circles: DNS in a horizontally periodic domain (Aguirre Guzmán *et al.* 2020).

and are included with dots. Numerical and experimental results corresponding to a smaller cylindrical convection cell at $Ra \approx 10^9$ and $Ek \approx 3 \times 10^{-6}$–$10^{-3}$ taken from Kunnen, Geurts & Clercx (2010) and Rajaei *et al.* (2018) are included with up and down triangles. Finally, the DNS study by Aguirre Guzmán *et al.* (2020) on a horizontally periodic domain with no-slip walls on bottom and top at $Ra = 5 \times 10^9$–10^{12} and $Ek \approx 10^{-7}$ is included with open circles. From figure 5, we can make several observations.

First, the plateauing at low Ra that we observed in figure 3(*a*) is also observed in the data of Hawkins *et al.* (2023). On the contrary, the simulation results on horizontally periodic domains (Aguirre Guzmán *et al.* 2020; Maffei *et al.* 2021) do not show such a plateau. The principal distinguishing property is the presence or absence of a sidewall. We know that the sidewall circulation generates jet-like intrusions from the sidewall region into the bulk (Favier & Knobloch 2020; Madonia *et al.* 2021). It is thus plausible that the observed plateauing of Re_w is caused by the dominance of the jets emerging from the sidewall circulation over the columnar convection in the central region. Note that the difference between the DNS of Aguirre Guzmán *et al.* (2020) and the asymptotic model of Maffei *et al.* (2021) at low $\widetilde{Ra} = Ra\,Ek^{4/3}$ is related to the applied boundary conditions: in this range, paradoxically, no-slip boundaries lead to higher Nu (and thus also higher Re_w) than stress-free boundaries at otherwise identical parameter values (Schmitz & Tilgner 2010; Stellmach *et al.* 2014; Kunnen *et al.* 2016; Plumley *et al.* 2017). This effect has been ascribed to the prevalence of Ekman pumping as a source of vertical transport, present for no-slip plates but absent for stress-free.

Second, the Reynolds number scaling depends sensitively on the magnitudes of Ra and Ek. The smaller-scale cylinder investigations of Kunnen *et al.* (2010) and Rajaei *et al.* (2018) at moderate $Ra \approx 10^9$ and Ek down to 3×10^{-6} display a significantly shallower slope than the larger cylinders (larger Ra and smaller Ek) of Hawkins *et al.* (2023)

and the current study. There is definitely a different scaling upon entering the geostrophic regime of rotating convection. In fact, these four studies together display a gradual transition as a function of both *Ra* and *Ek*. A steeper scaling can be seen as *Ek* is reduced, while concomitantly increasing *Ra* to retain turbulent convection, save for the added complications due to the sidewall circulation.

Third, the smallest-*Ek* data points (orange and red) display a trend towards convergence to the asymptotic results for $(Ra - Ra_C)\, Ek^{4/3}/Pr \gtrsim 50$ and $Re_w\, Ek^{1/3} \gtrsim 20$. Notably, results of completely different origin (experiments, DNS and asymptotic models; horizontally periodic domains and confined cylinders) display convergence towards a common scaling behaviour. Based on this convergence, we expect that the effect of the wall modes on the Re_w scaling is minimal. A linear scaling in figure 5 corresponds directly to the relation expressed in (2.17) where the velocity scale becomes independent of both diffusive parameters and domain-specific parameters, such as its height *H*. The convergence is not yet fully achieved; extra data points at even smaller *Ek* values are required to corroborate this, but tough to realise experimentally or numerically. Such investigations may also allow us to investigate further the possible convergence between the curves coming from asymptotically reduced simulations, full Navier–Stokes simulations and experiments. We note that the asymptotic simulations of Maffei *et al.* (2021) in fact result in stronger-than-linear scaling $\widetilde{Re}_w \sim \widetilde{Ra}^{1.2}$ (at $Pr = 1$), which shows additionally that the existence of true diffusion-free flow behaviour remains an open question.

5. Energy spectra

To compute the energy spectra, we employ two-dimensional fast Fourier transforms of the velocity field, after padding the vector fields with zeros up to 512 grid points per dimension to avoid artefacts due to implied periodicity in the Fourier transform (Randall 2008). The two-dimensional data are averaged over circular shells to obtain one representative curve independent of azimuthal angle. Since adjacent velocity vectors are $\Delta x = 3.2$ mm apart, the smallest wavenumber after zero padding is $k_{\mathcal{L}} = 2\pi/\mathcal{L} = 2\pi/(512\,\Delta x) \approx 3.83$ m^{-1}, and the maximum relevant *k* value (Nyquist wavenumber) is $k_{2\Delta x} = 2\pi/(2\,\Delta x) \approx 982$ m^{-1}. All the *k* values are integer multiples of $k_{\mathcal{L}}$. Nevertheless, the smallest physically relevant *k* is determined by the diameter *D* of the cylinder; that would be given by $k_D = 2\pi/D \approx 16.1$ m^{-1}, but since all the wavenumbers are integer multiples of $k_{\mathcal{L}}$, our first relevant value is $k_{min} \approx 19.2$ m^{-1} – in dimensionless form, $k_{min}H \approx 38.4$.

The maximum relevant *k* requires more consideration. Previous literature (Foucaut, Carlier & Stanislas 2004; Savelsberg 2006) has shown that the window averaging applied in PIV measurements acts as a low-pass filter in Fourier space with a cut-off wavenumber that depends on the size of the measurement window *X* (in our case, $X = 2\,\Delta x = 6.4$ mm). The PIV filtering amounts to a multiplication in Fourier space of the real signal with a squared cardinal sine function

$$\text{sinc}^2(kX/2) = \left(\frac{\sin kX/2}{kX/2}\right)^2. \tag{5.1}$$

We can then correct for this filtering, with corrected energy spectra becoming

$$E_{corr} = \frac{E_{meas}}{\text{sinc}^2(kX/2)}, \tag{5.2}$$
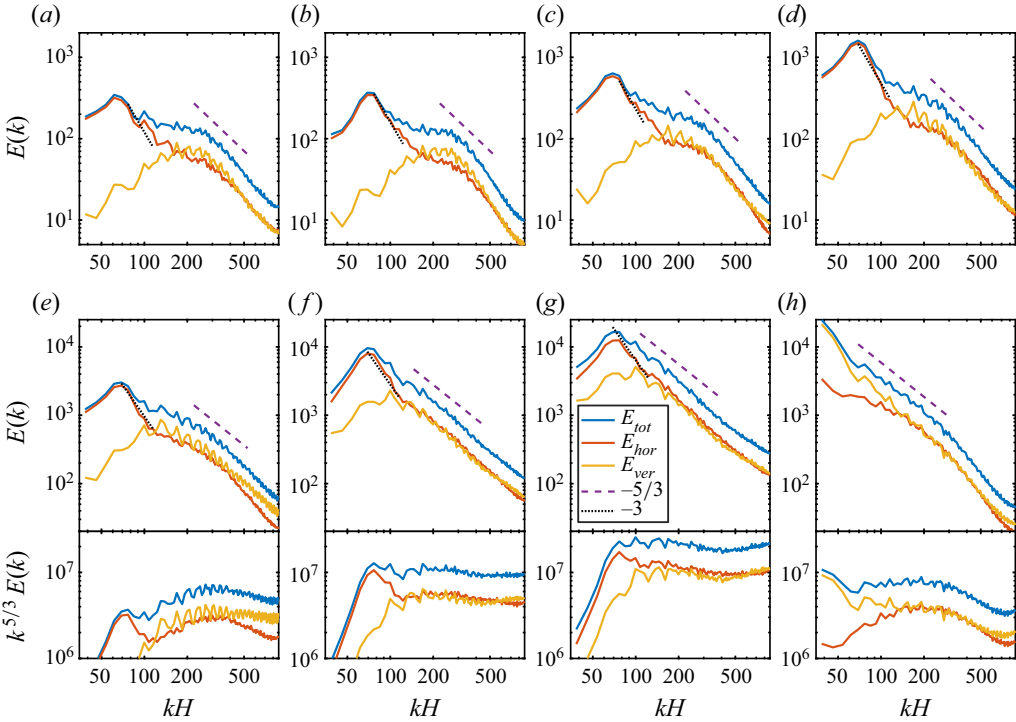
Figure 6. Kinetic energy spectra $E(k)$ plotted as functions of normalised wavenumber kH, including total kinetic energy (E_{tot}) as well as the contributions from horizontal (E_{hor}) and vertical (E_{ver}) velocity components. Reference power-law slopes $k^{-5/3}$ and k^{-3} are also included. Graphs (*e–h*) are also plotted in compensated form $k^{5/3} E(k)$.

where E_{meas} is the uncorrected spectrum determined directly from the PIV data, and E_{corr} is the corrected spectrum. However, given that $\mathrm{sinc}^2(kX/2) \to 0$ as $kX/2 \to \pi$, direct application of (5.2) may cause practical difficulties: measurement noise will be severely amplified when approaching the zero of the denominator. To deal with this, we employ the rule of thumb proposed by Foucaut *et al.* (2004) to cut off the spectra at a maximum $k_{max} = 2.8/X$. At this k value, the filter function is $\mathrm{sinc}^2(k_{max}X/2) \approx 0.5$, i.e. the spectrum is cut off at the wavenumber k_{max} where PIV filtering reduces the measured spectral amplitude by 50 %. In our case, $k_{max}H = 874$.

In figure 6, we show the energy spectra of our seven RRBC cases as well as the non-rotating case. We plot the total energy spectrum (E_{tot}) together with the respective contributions from the horizontal (E_{hor}) and vertical (E_{ver}) velocity components. Wavenumbers are normalised using the cell height H.

The rotating cases show common features. In all of them, E_{tot} exhibits a peak at $kH \approx 70$, which corresponds to the physical wavelength $L \approx 0.18$ m $\approx D/2$. This peak is related to the ordering into a quadrupolar vortex state that we reported before (Madonia *et al.* 2021), which in hindsight was also found in the mean flow fields of de Wit *et al.* (2020). Ecke *et al.* (2022) also show this flow organisation in their figure 2(*c*). Jets pointing radially inwards are observed at the positions where upward and downward flowing parts of the sidewall circulation meet, resulting in a four-quadrant organisation with two cyclonic and two anticyclonic vortices. The formation of these jets is a nonlinear feature of the sidewall circulation absent from its linear description (Herrmann & Busse 1993;

Liao, Zhang & Chang 2006; Zhang & Liao 2009). The dependence on the geometrical aspect ratio Γ is an open question; we do anticipate changes for wider cylinders where more than one azimuthal wavelength can fit into the circumference. Here, with one azimuthal wavelength, we see an organisation into a quadrupolar vortex where each pole has characteristic size $L \approx D/2$. These structures are most energetic, but at the same time they are quasi-two-dimensional: there is no signature of them in the spectra E_{ver} based on vertical velocity.

The shape of the remaining part of each spectrum is strongly dependent on the vertical energy contribution. As Ra increases, the peak in E_{ver} goes towards smaller k (larger length scales), a feature that we have observed before (Madonia *et al.* 2021) from calculations of the characteristic horizontal correlation length scale based on vertical velocity. We interpret this as the scale at which buoyancy is most prominently adding energy into the turbulent motion. In the language of the classical theory of three-dimensional turbulence (e.g. Frisch 1995; Pope 2000), this scale can be considered the forcing scale. The dissipation scale (i.e. the Kolmogorov scale) remains approximately constant, leading to increased scale separation between forcing and dissipation as Ra becomes larger. From the maximum of E_{ver} towards larger k values, we see the gradual development of a spectral scaling range close to $E(k) \sim k^{-5/3}$, the predicted scaling for the inertial range of three-dimensional turbulence (Frisch 1995; Pope 2000). This scaling range is most prominent in the E_{tot} curves and at larger Ra. We also plot the spectra of figures 6(*e–h*) in a compensated form $k^{5/3}E(k)$ to show the quality and extent of the $k^{-5/3}$ scaling range: the scaling range is not well developed in figure 6(*e*) at $Ra = 1.08 \times 10^{12}$, but it is present prominently in figures 6(*f–h*), the two rotating convection experiments at larger Ra and the non-rotating case at $Ra = 6.48 \times 10^{11}$. Figures 6(*a–d*) are not shown in compensated form as no scaling range develops there.

The sum of horizontal and vertical contributions is reflected clearly in the total spectra E_{tot}, with the peak due to the quadrupolar vortex dominating at smaller k, and a broad shoulder due to the peak contribution of E_{ver} that shifts as a function of Ra.

The horizontal spectra, in fact, also show a different scaling trend, from the approximate location of the peak of E_{ver} to smaller wavenumbers ending on the maximum of E_{hor}, which resembles the $E(k) \sim k^{-3}$ scaling. This k^{-3} scaling could be a sign of a (non-local) inverse cascade (Smith & Waleffe 1999; Lindborg 2007; Julien *et al.* 2012*b*; Aguirre Guzmán *et al.* 2020), although this scaling range is short and certainly cannot be considered as a proof. We are investigating the energy transfer among scales in more detail.

The non-rotating RBC case, instead, shows a very different situation. The peak of the overall spectrum is at k_{min}, and it is due dominantly to the contribution of E_{ver}. It is a sign of the presence of the large-scale circulation of non-rotating convection (e.g. Ahlers *et al.* 2009): a domain-filling vertical convection roll with one half of the domain displaying upward flow and the other half downward. We have observed it in the current measurements (Madonia *et al.* 2021; Madonia 2022). This structure corresponds to a wavelength of approximately the diameter of the cylinder, that in wavenumber space is translated to k_{min}. Here, we also observe a rather extensive scaling range nicely matching the theoretical prediction $k^{-5/3}$.

6. Conclusion

We present flow statistics that result from the stereo-PIV measurements of rotating Rayleigh–Bénard convection in the geostrophic regime. We analyse radial profiles of the root-mean-square values of horizontal and vertical velocity as well as vertical vorticity.

Near the sidewall, the radial extent of the sidewall circulation can be distinguished clearly. We see that for both velocities and vorticities, higher *Ra* corresponds to larger values of these quantities, and at the same *Ra*, the non-rotating case exhibits larger magnitudes than the corresponding rotating one.

Within the bulk region, for the flow states from plumes to rotation-influenced turbulence (RIT), the Reynolds number scalings follow a trend that lies in the range of both CIA and VAC scaling predictions, perhaps being numerically closer to the former, but otherwise no decisive distinction can be made. The vorticity scaling follows the same trend as the horizontal velocity, indicating that the characteristic horizontal scale remains constant (e.g. Sprague *et al.* 2006; Julien *et al.* 2012*b*; Madonia *et al.* 2021). We also find that energy is distributed nearly isotropically, in contrast to non-rotating Rayleigh–Bénard convection where the vertical velocity component is strongly preferred.

The Reynolds number results compared to previously published results reveal that there is an overall steepening trend towards 'ultimate' diffusion-free scaling (Aurnou *et al.* 2020) of the velocity fluctuations as the Ekman number is reduced, but we do not reach it yet. However, there are indications of convergence in scaling for results coming from different methods (experiments, direct numerical simulations and asymptotically reduced models) and different geometries (confined cylinders and horizontally periodic computational domains). At lower *Ra*, there are complications due to the use of a confined geometry, as it promotes the presence of a wall mode that affects the bulk flow statistics.

Spectra of kinetic energy provide further evidence for the formation of a prominent quadrupolar vortex structure (Madonia *et al.* 2021). This feature is remarkably two-dimensional, as it is reflected only in spectra of horizontal velocity. In the spectra of vertical velocity, we observe a broad peak that we associate with the dominant length scale for energy injection. With increasing *Ra*, the peak shifts towards smaller wavenumbers (larger length scales; Madonia *et al.* 2021). For larger wavenumbers, we observe the development of a scaling range with a classical $-5/3$ slope for three-dimensional turbulence (Frisch 1995; Pope 2000). This inertial range scaling is most prominent for the non-rotating case.

These results provide valuable input on the turbulence scaling of flows in the geostrophic regime, a property that has been scarcely investigated up to now. There is clear perspective in the observed convergence of results from significantly different domains and employing different methods. At the same time, to reach true convergence, even more extreme parameter values than those used here are likely required, which is a major challenge for both experiments and direct numerical simulations. Additionally, the influence of the strong convection mode near the sidewall, the sidewall circulation, should be explored further to ensure proper interpretation of experimental and numerical results from confined domains.

Data availability statement. The data that support the findings of this study are available from the corresponding author, R.P.J.K., upon reasonable request.

Declaration of interests. The authors report no conflict of interest.

Author ORCIDs.
Ⓓ Matteo Madonia https://orcid.org/0000-0002-8510-8103;
Ⓓ Andrés J. Aguirre Guzmán https://orcid.org/0000-0002-4942-5216;

🔘 Herman J.H. Clercx https://orcid.org/0000-0001-8769-0435;

🔘 Rudie P.J. Kunnen https://orcid.org/0000-0002-1219-694X.

REFERENCES

AGUIRRE GUZMÁN, A.J., MADONIA, M., CHENG, J.S., OSTILLA-MÓNICO, R., CLERCX, H.J.H. & KUNNEN, R.P.J. 2020 Competition between Ekman plumes and vortex condensates in rapidly rotating thermal convection. *Phys. Rev. Lett.* **125**, 214501.

AGUIRRE GUZMÁN, A.J., MADONIA, M., CHENG, J.S., OSTILLA-MÓNICO, R., CLERCX, H.J.H. & KUNNEN, R.P.J. 2021 Force balance in rapidly rotating Rayleigh–Bénard convection. *J. Fluid Mech.* **928**, A16.

AGUIRRE GUZMÁN, A.J., MADONIA, M., CHENG, J.S., OSTILLA-MÓNICO, R., CLERCX, H.J.H. & KUNNEN, R.P.J. 2022 Flow- and temperature-based statistics characterizing the regimes in rapidly rotating turbulent convection in simulations employing no-slip boundary conditions. *Phys. Rev. Fluids* **7**, 013501.

AHLERS, G., GROSSMANN, S. & LOHSE, D. 2009 Heat transfer and large scale dynamics in turbulent Rayleigh–Bénard convection. *Rev. Mod. Phys.* **81**, 503–537.

AUBERT, J., BRITO, D., NATAF, H.-C., CARDIN, P. & MASSON, J.-P. 2001 A systematic experimental study of rapidly rotating spherical convection in water and liquid gallium. *Phys. Earth Planet. Inter.* **128**, 51–74.

AURNOU, J.M., BERTIN, V., GRANNAN, A.M., HORN, S. & VOGT, T. 2018 Rotating thermal convection in liquid gallium: multi-modal flow, absent steady columns. *J. Fluid Mech.* **846**, 846–876.

AURNOU, J.M., CALKINS, M.A., CHENG, J.S., JULIEN, K., KING, E.M., NIEVES, D., SODERLUND, K.M. & STELLMACH, S. 2015 Rotating convective turbulence in Earth and planetary cores. *Phys. Earth Planet. Inter.* **246**, 52–71.

AURNOU, J.M., HORN, S. & JULIEN, K. 2020 Connections between nonrotating, slowly rotating, and rapidly rotating turbulent convection transport scalings. *Phys. Rev. Res.* **2**, 043115.

BOUBNOV, B.M. & GOLITSYN, G.S. 1990 Temperature and velocity field regimes of convective motions in a rotating plane fluid layer. *J. Fluid Mech.* **219**, 215–239.

BOUILLAUT, V., MIQUEL, B., JULIEN, K., AUMAÎTRE, S. & GALLET, B. 2021 Experimental observation of the geostrophic turbulence regime of rapidly rotating convection. *Proc. Natl Acad. Sci. USA* **118**, e2105015118.

CHANDRASEKHAR, S. 1961 *Hydrodynamic and Hydromagnetic Stability*. Oxford University Press.

CHENG, J.S., AURNOU, J.M., JULIEN, K. & KUNNEN, R.P.J. 2018 A heuristic framework for next-generation models of geostrophic convective turbulence. *Geophys. Astrophys. Fluid Dyn.* **112**, 277–300.

CHENG, J.S., MADONIA, M., AGUIRRE GUZMÁN, A.J. & KUNNEN, R.P.J. 2020 Laboratory exploration of heat transfer regimes in rapidly rotating turbulent convection. *Phys. Rev. Fluids* **5**, 113501.

CHENG, J.S., STELLMACH, S., RIBEIRO, A., GRANNAN, A., KING, E.M. & AURNOU, J.M. 2015 Laboratory-numerical models of rapidly rotating convection in planetary cores. *Geophys. J. Intl* **201**, 1–17.

ECKE, R.E. & NIEMELA, J.J. 2014 Heat transport in the geostrophic regime of rotating Rayleigh–Bénard convection. *Phys. Rev. Lett.* **113**, 114301.

ECKE, R.E. & SHISHKINA, O. 2023 Turbulent rotating Rayleigh–Bénard convection. *Annu. Rev. Fluid Mech.* **55**, 603–638.

ECKE, R.E., ZHANG, X. & SHISHKINA, O. 2022 Connecting wall modes and boundary zonal flows in rotating Rayleigh–Bénard convection. *Phys. Rev. Fluids* **7**, L011501.

FAVIER, B. & KNOBLOCH, E. 2020 Robust wall states in rapidly rotating Rayleigh–Bénard convection. *J. Fluid Mech.* **895**, R1.

FOUCAUT, J.-M., CARLIER, J. & STANISLAS, M. 2004 PIV optimization for the study of turbulent flow using spectral analysis. *Meas. Sci. Technol.* **15**, 1046–1058.

FRISCH, U. 1995 *Turbulence: The Legacy of A.N. Kolmogorov*. Cambridge University Press.

GILLET, N. & JONES, C. 2006 The quasi-geostrophic model for rapidly rotating spherical convection outside the tangent cylinder. *J. Fluid Mech.* **554**, 343–369.

GLATZMAIER, G.A. 2014 *Introduction to Modeling Convection in Planets and Stars. Magnetic Field, Density Stratification, Rotation*. Princeton University Press.

GREENSPAN, H.P. 1968 *The Theory of Rotating Fluids*. Cambridge University Press.

GROSSMANN, S. & LOHSE, D. 2000 Scaling in thermal convection: a unifying theory. *J. Fluid Mech.* **407**, 27–56.

GROSSMANN, S. & LOHSE, D. 2001 Thermal convection for large Prandtl numbers. *Phys. Rev. Lett.* **86**, 3316–3319.

GROSSMANN, S. & LOHSE, D. 2002 Prandtl and Rayleigh number dependence of the Reynolds number in turbulent thermal convection. *Phys. Rev.* E **66**, 016305.

GROSSMANN, S. & LOHSE, D. 2004 Fluctuations in turbulent Rayleigh–Bénard convection: the role of plumes. *Phys. Fluids* **16**, 4462–4472.

GUERVILLY, C., CARDIN, P. & SCHAEFFER, N. 2019 Turbulent convective length scale in planetary cores. *Nature* **570**, 368–371.

HAWKINS, E.K. 2020 Experimental investigations of convective turbulence in planetary cores. PhD thesis, University of California Los Angeles, Los Angeles, CA, USA.

HAWKINS, E.K., CHENG, J.S., ABBATE, J.A., PILEGARD, T., STELLMACH, S., JULIEN, K. & AURNOU, J.M. 2023 Laboratory models of planetary core-style convective turbulence. *Fluids* **8**, 106.

HERRMANN, J. & BUSSE, F.H. 1993 Asymptotic theory of wall-attached convection in a rotating fluid layer. *J. Fluid Mech.* **255**, 183–194.

HORN, S. & AURNOU, J.M. 2018 Regimes of Coriolis–centrifugal convection. *Phys. Rev. Lett.* **120**, 204502.

HORN, S. & AURNOU, J.M. 2019 Rotating convection with centrifugal buoyancy: numerical predictions for laboratory experiments. *Phys. Rev. Fluids* **4**, 073501.

INGERSOLL, A. & POLLARD, D. 1982 Motion in the interiors and atmospheres of Jupiter and Saturn: scale analysis, anelastic equations, barotropic stability criterion. *Icarus* **52**, 62–80.

JONES, C.A. 2011 Planetary magnetic fields and fluid dynamos. *Annu. Rev. Fluid Mech.* **43**, 583–614.

JULIEN, K., KNOBLOCH, E., RUBIO, A.M. & VASIL, G.M. 2012*a* Heat transport in low-Rossby-number Rayleigh–Bénard convection. *Phys. Rev. Lett.* **109**, 254503.

JULIEN, K., RUBIO, A.M., GROOMS, I. & KNOBLOCH, E. 2012*b* Statistical and physical balances in low Rossby number Rayleigh–Bénard convection. *Geophys. Astrophys. Fluid Dyn.* **106**, 392–428.

KING, E.M., STELLMACH, S. & AURNOU, J.M. 2012 Heat transfer by rapidly rotating Rayleigh–Bénard convection. *J. Fluid Mech.* **691**, 568–582.

KING, E.M., STELLMACH, S. & BUFFETT, B. 2013 Scaling behaviour in Rayleigh–Bénard convection with and without rotation. *J. Fluid Mech.* **717**, 449–471.

KING, E.M., STELLMACH, S., NOIR, J., HANSEN, U. & AURNOU, J.M. 2009 Boundary layer control of rotating convection systems. *Nature* **457**, 301–304.

KRAICHNAN, R.H. 1962 Turbulent thermal convection at arbitrary Prandtl number. *Phys. Fluids* **5**, 1374–1389.

KUNDU, P.K. & COHEN, I.M. 2002 *Fluid Mechanics*, 2nd edn. Academic.

KUNNEN, R.P.J. 2021 The geostrophic regime of rapidly rotating turbulent convection. *J. Turbul.* **22**, 267–296.

KUNNEN, R.P.J., GEURTS, B.J. & CLERCX, H.J.H. 2010 Experimental and numerical investigation of turbulent convection in a rotating cylinder. *J. Fluid Mech.* **642**, 445–476.

KUNNEN, R.P.J., OSTILLA-MÓNICO, R., VAN DER POEL, E.P., VERZICCO, R. & LOHSE, D. 2016 Transition to geostrophic convection: the role of the boundary conditions. *J. Fluid Mech.* **799**, 413–432.

LIAO, X., ZHANG, K. & CHANG, Y. 2006 On boundary-layer convection in a rotating fluid. *J. Fluid Mech.* **549**, 375–384.

LINDBORG, E. 2007 Third-order structure function relations for quasi-geostrophic turbulence. *J. Fluid Mech.* **572**, 47–85.

LU, H.-Y., DING, G.-Y., SHI, J.-Q., XIA, K.-Q. & ZHONG, J.-Q. 2021 Heat-transport scaling and transition in geostrophic rotating convection with varying aspect ratio. *Phys. Rev. Fluids* **6**, L071501.

MADONIA, M. 2022 Laboratory study of rotation-dominated convective turbulence. PhD thesis, Eindhoven University of Technology, Eindhoven, The Netherlands.

MADONIA, M., AGUIRRE GUZMÁN, A.J., CLERCX, H.J.H. & KUNNEN, R.P.J. 2021 Velocimetry in rapidly rotating convection: spatial correlations, flow structures and length scales. *Europhys. Lett.* **135**, 54002.

MAFFEI, S., KROUSS, M.J., JULIEN, K. & CALKINS, M.A. 2021 On the inverse cascade and flow speed scaling behavior in rapidly rotating Rayleigh–Bénard convection. *J. Fluid Mech.* **913**, A18.

MALKUS, W.V.R. 1954 The heat transport and spectrum of thermal turbulence. *Proc. R. Soc. Lond.* A **225**, 196–212.

NIILER, P.P. & BISSHOPP, F.E. 1965 On the influence of Coriolis forces on onset of thermal convection. *J. Fluid Mech.* **22**, 753–761.

PLUMLEY, M., JULIEN, K., MARTI, P. & STELLMACH, S. 2017 Sensitivity of rapidly rotating Rayleigh–Bénard convection to Ekman pumping. *Phys. Rev. Fluids* **2**, 094801.

POPE, S.B. 2000 *Turbulent Flows*. Cambridge University Press.

PRASAD, A.K. 2000 Stereoscopic particle image velocimetry. *Exp. Fluids* **29**, 103–116.

RAFFEL, M., WILLERT, C.E., WERELEY, S.T. & KOMPENHANS, J. 2007 *Particle Image Velocimetry*, 2nd edn. Springer.

RAJAEI, H., ALARDS, K.M.J., KUNNEN, R.P.J. & CLERCX, H.J.H. 2018 Velocity and acceleration statistics in rapidly rotating Rayleigh–Bénard convection. *J. Fluid Mech.* **857**, 374–397.

RANDALL, R.B. 2008 Spectral analysis and correlation. In *Handbook of Signal Processing in Acoustics* (ed. D. Havelock, S. Kuwano & M. Vorländer), pp. 33–52. Springer.

SAVELSBERG, R. 2006 Experiments on free-surface turbulence. PhD thesis, Eindhoven University of Technology, Eindhoven, The Netherlands.

SCHMITZ, S. & TILGNER, A. 2010 Transitions in turbulent rotating Rayleigh–Bénard convection. *Geophys. Astrophys. Fluid Dyn.* **104**, 481–489.

SCHUMACHER, J. & SREENIVASAN, K.R. 2020 Colloquium: unusual dynamics of convection in the Sun. *Rev. Mod. Phys.* **92**, 041001.

SHRAIMAN, B.I. & SIGGIA, E.D. 1990 Heat transport in high-Rayleigh-number convection. *Phys. Rev.* A **42**, 3650–3653.

SMITH, L. & WALEFFE, F. 1999 Transfer of energy to two-dimensional large scales in forced, rotating three-dimensional turbulence. *Phys. Fluids* **11**, 1608–1622.

SPIEGEL, E.A. 1971 Convection in stars: I. Basic Boussinesq convection. *Annu. Rev. Astron. Astrophys.* **9**, 323–352.

SPRAGUE, M., JULIEN, K., KNOBLOCH, E. & WERNE, J. 2006 Numerical simulation of an asymptotically reduced system for rotationally constrained convection. *J. Fluid Mech.* **551**, 141–174.

STELLMACH, S., LISCHPER, M., JULIEN, K., VASIL, G., CHENG, J.S., RIBEIRO, A., KING, E.M. & AURNOU, J.M. 2014 Approaching the asymptotic regime of rapidly rotating convection: boundary layers versus interior dynamics. *Phys. Rev. Lett.* **113**, 254501.

STEVENS, R.J.A.M., CLERCX, H.J.H. & LOHSE, D. 2013*a* Heat transport and flow structure in rotating Rayleigh–Bénard convection. *Eur. J. Mech.* (B*/Fluids*) **40**, 41–49.

STEVENS, R.J.A.M., VAN DER POEL, E.P., GROSSMANN, S. & LOHSE, D. 2013*b* The unifying theory of scaling in thermal convection: the updated prefactors. *J. Fluid Mech.* **730**, 295–308.

STEVENSON, D.J. 1979 Turbulent thermal convection in the presence of rotation and a magnetic field: a heuristic theory. *Geophys. Astrophys. Fluid Dyn.* **12**, 139–169.

WEDI, M., MOTURI, V.M., FUNFSCHILLING, D. & WEISS, S. 2022 Experimental evidence for the boundary zonal flow in rotating Rayleigh–Bénard convection. *J. Fluid Mech.* **939**, A14.

DE WIT, X.M., AGUIRRE GUZMÁN, A.J., MADONIA, M., CHENG, J.S., CLERCX, H.J.H. & KUNNEN, R.P.J. 2020 Turbulent rotating convection confined in a slender cylinder: the sidewall circulation. *Phys. Rev. Fluids* **5**, 023502.

YAN, M. & CALKINS, M.A. 2022 Asymptotic behaviour of rotating convection-driven dynamos in the plane layer geometry. *J. Fluid Mech.* **951**, A24.

ZHANG, X., ECKE, R.E. & SHISHKINA, O. 2021 Boundary zonal flows in rapidly rotating turbulent thermal convection. *J. Fluid Mech.* **915**, A62.

ZHANG, X., VAN GILS, D.P.M., HORN, S., WEDI, M., ZWIRNER, L., AHLERS, G., ECKE, R.E., WEISS, S., BODENSCHATZ, E. & SHISHKINA, O. 2020 Boundary zonal flow in rotating turbulent Rayleigh–Bénard convection. *Phys. Rev. Lett.* **124**, 084505.

ZHANG, K. & LIAO, X. 2009 The onset of convection in rotating circular cylinders with experimental boundary conditions. *J. Fluid Mech.* **622**, 63–73.